

Concentration and temperature dependent double energy gap characteristic properties of hexagonal $\text{YMnO}_3-x\text{BiFeO}_3$ films

This content has been downloaded from IOPscience. Please scroll down to see the full text.

2016 J. Phys. D: Appl. Phys. 49 465302

(<http://iopscience.iop.org/0022-3727/49/46/465302>)

View [the table of contents for this issue](#), or go to the [journal homepage](#) for more

Download details:

IP Address: 222.66.117.13

This content was downloaded on 26/10/2016 at 05:13

Please note that [terms and conditions apply](#).

Concentration and temperature dependent double energy gap characteristic properties of hexagonal $\text{YMnO}_3-x\text{BiFeO}_3$ films

Z Xu, Q L Deng, P Zhang, J Z Zhang, Y W Li, Z G Hu and J H Chu

Technical Center for Multifunctional Magneto-Optical Spectroscopy (ECNU), Shanghai
Department of Electronic Engineering, East China Normal University, Shanghai 200241,
People's Republic of China

E-mail: zghu@ee.ecnu.edu.cn

Received 16 July 2016, revised 21 September 2016

Accepted for publication 23 September 2016

Published 24 October 2016



Abstract

The study of hexagonal $(1-x)\text{YMnO}_3-x\text{BiFeO}_3$ ($0 \leq x \leq 2.5\%$) (YBMF x) films can realize the modulation of h -YMO films, especially for the significant modulation of crystal orientation and surface. The choice of the solvent and solution, and the co-doping of Fe and Bi are two important facts of realizing the modulation. The results of x-ray diffraction and atomic force microscopy measurements indicated that there are the internal relations of the lattice orientation and the surface morphology for highly c -axis-orientation (HCO) and no preferred orientation (NPO), respectively. X-ray photoelectron spectroscopy confirmed that manganese ions show a valence of +3 in YMnO_3 film. The peak positions of the Mn $2p$ level move to higher energy with increasing concentration. Furthermore, there is an optimal doping concentration of $x = 1.5\%$ for the YBMF x ($0 \leq x \leq 2.5\%$) films by taking the shapes of P - E loops, the values of $2P_r$ and $2E_c$ into consideration. The transmittance spectra at room temperature pointed out that the double energy gaps (~ 1.25 eV and 3.3 eV) corresponded to significant absorption edges, the band gap (E_{g1}) and subband gap (E_{g2}), respectively. The different dependency of E_{g1} at the lower temperature can be explained by the ionized impurity scattering. A critical temperature (~ 100 K) of E_{g2} can be attributed to the relaxation of antiferromagnetic phase transformation. The abnormal shrinkage of E_{g2} below 100 K can be explained by the pinning effect of composite domain walls and the accumulation of discrete oxygen vacancies at composite domain walls. The present study sheds light on the understanding of the electronic band structure, antiferromagnetic phase transformation and their relation in h -YMO. Moreover, it contributes to the verification and improvement of Katsufuji's model (Katsufuji *et al* 2001 *Phys. Rev. B* **64** 104419).

Keywords: $\text{YMnO}_3-x\text{BiFeO}_3$, temperature dependence, double energy gap, spectral transmittance

(Some figures may appear in colour only in the online journal)

1. Introduction

Multiferroic materials, often possessing more than one simultaneous ferroic order, have been extensively studied over the past decade due to the potential application of spintronics and memory devices [1–3]. Recently, hexagonal YMnO_3 (h -YMO), an important multiferroic material due to the coupling of the antiferromagnetic and ferroelectric, attracted a

great deal of research interest. [4–9] For h -YMO, each Mn^{3+} ion ($3d^4$) with total spin quantum number $S = 2$ is surrounded by three in-plane and two apical oxygen ions, submitting naturally to a trigonal crystal field [10, 11]. These MnO_5 blocks are mutually connected two-dimensionally on their corners, in favour of forming a triangular network of Mn^{3+} ions. It is generally believed that antiferromagnetic is derived from a triangular lattice of Mn^{3+} ions, and ferroelectricity is derived from

the distortion of Y^{3+} ions in *h*-YMO [12]. Besides, *h*-YMO is room temperature ferroelectric with the Curie temperature of about 900 K and low temperature antiferromagnetic with the Néel temperature of about 70 K [11, 13]. There are the corresponding ferroelectric domain and antiferromagnetic domain structure, simultaneously. Moreover, the band gap of *h*-YMO is about 1.5 eV [8, 14, 15], which approaches that of Si (~ 1.1 eV) and that of GaAs (~ 1.4 eV) [16, 17]. The dielectric constant of single-crystal *h*-YMO is about 20 [18], which is close to that of Si (~ 12) [19, 20]. It is suitable as a ferroelectric material in a metal/ferroelectric/insulator/semiconductor structure (MFIS) [18]. These features of *h*-YMO provided the possibility for better developing the ferroelectric memory based on a silicon integrated circuit.

The electronic band structure of *h*-YMO as a function of temperature often has an important referent value for the research on antiferromagnetic phase transformation. Recently, Katsufuji *et al* [21] reported that the dielectric abnormality was caused by the magnetic-ordering-dependent electronic excitation gap (E_g) in the *ab*-plane due to the coupling of the antiferromagnetism and the dielectric properties. In fact, the *h*-YMO has a Mn-O triangular bipyramid cage, and two E_{1g} orbitals d_{yz} and d_{zx} form the lowest level, followed by two E_{2g} orbitals d_{xy} and $d_{x^2-y^2}$, and the a_{1g} orbital $d_{3z^2-r^2}$. According to optical conductivity spectra and theoretical calculation [22], the E_{g1} and E_{g2} of YMO could be attributed to the gap between two hybridized bands. One is from the hybridization between in-plane O $2p$ orbitals and the related Mn E_{2g}/E_{1g} orbitals, and the other is from the hybridization between apical O $2p$ orbitals and the related Mn a_{1g} orbitals. Therefore, antiferromagnetic phase transformation has a possible influence on E_{g1} and E_{g2} . It can be attributed to the possible modulation of hybridization between in-plane O $2p$ orbitals and the relevant Mn E_{2g}/E_{1g} orbitals. However, the influence was ignored for Katsufuji's mode. Moreover, there has been few studies of temperature dependent double energy gaps of *h*-YMO. Thus, it is desired to explore the temperature dependent double energy gaps of *h*-YMO. It is hoped that the direct evidence of modulation on the band gap and other energy gaps can be found by the variable temperature transmission.

How to get a higher uniaxial ferroelectric orientational *h*-YMO is a critical challenging for the potential applications of *h*-YMO. For a long time, the higher uniaxial ferroelectric orientational *h*-YMO could be received by the floating zone melting process [5], pulsed laser deposition (PLD) [9, 23] and molecular beam epitaxy (MBE) [24], which are not conducive to the popularization and application due to the exorbitant price. The traditional solid phase sintering method can bring out the poor surface and electrical deterioration, especially, for larger leakage current. It is related to the larger anisotropic of the thermal expansion coefficient, which often leads to the micron grade crack at the high temperature preparation or the subsequent heat treatment [25, 26]. The insulating substrates and insulating buffer layers usually are used to decrease the leakage current [27]. Choi *et al* reported that the highly *c*-axis-oriented growth of quality Bi doped *h*-YMO films were acquired by PLD at lower temperature [28]. However, the

effective Bi concentration above 5% brings out the significant Bi_2O_3 surface layer. In addition, the influence of Fe doped on antiferromagnetic phase transformation of *h*-YMO has been studied [29, 30]. However, the modulation of Fe doped on crystal and surface layer was rarely mentioned. Note that the sol-gel method is a well-accepted method due to some evident advantages, such as its chemical homogeneity, ease of stoichiometry control, low-cost and suitability for mass production [31, 32]. It is hoped that the sol-gel films of Fe and Bi co-doping can realize the controlled growth of *h*-YMO, especially, for the significant modulation of crystal orientation.

In this work, crystallographic excellent $(1-x)YMnO_3-xBiFeO_3$ ($0 \leq x \leq 2.5\%$) (YBMF x) polycrystalline films were successfully obtained by the sol-gel technique. The choice of solvent and solution, and the Fe and Bi co-doping realized the modulation of *h*-YMO films, including the significant modulation of crystal orientation and morphology. Electronic structure and ferroelectric properties were studied. The transmittance spectra provided the preliminary information of band energy for *h*-YMO film. The temperature dependent E_{g1} and E_{g2} were explored. A critical temperature (~ 100 K) of E_{g2} can be attributed to the relaxation of antiferromagnetic phase transformation. The study of the double energy gap for *h*-YMO is conducive to better understanding of the electronic band structure, antiferromagnetic phase transformation and their relation in *h*-YMO.

2. Experimental details

2.1. Fabrication of YBMF x films

The YBMF x ($0 \leq x \leq 2.5\%$) films on quartz substrates were prepared by the sol-gel technique. Analytically pure bismuth nitrate ($Bi(NO_3)_3 \cdot 5H_2O$, 99.0%), manganese acetate tetrahydrate ($Mn(CH_3COO)_2 \cdot 4H_2O$, 99.0%), yttrium nitrate hexahydrate ($Y(NO_3)_3 \cdot 6H_2O$, 99.0%), ferric nitrate ninehydrate ($Fe(NO_3)_3 \cdot 9H_2O$, 98.5%) were used as the starting materials. The required $Mn(CH_3COO)_2 \cdot 4H_2O$ and $Y(NO_3)_3 \cdot 6H_2O$ were mixed in the required molar ratio of manganese and yttrium and then dissolved in a mixture of ethylene glycol monomethylether ($C_3H_8O_2$, 99.0%), ethylene glycol ($C_2H_6O_2$, 99.0%) and acetic acid (CH_3COOH , 99.5%) with a volume ratio of 4:2:1. After the solution was stable and became transparent and homogeneous by magnetic stirring, the required Fe ($NO_3)_3 \cdot 9H_2O$ and $Bi(NO_3)_3 \cdot 5H_2O$ were added into the solution, and stirring was continuous until they were completely dissolved. Excess bismuth of about 10 mol% was used to compensate for bismuth loss during the annealing process. Finally, an appropriate amount of acetylacetone ($C_5H_8O_2$, 99.0%) was added to stabilize the solution. The solutions of YMO and YBMF2.5% can be obtained by the method mentioned above, and the other solutions were obtained by mixing the two solutions with different volume ratios. Magnetic stirring was carried out for 24 h, then the solutions were refluxed for 2–4 h. The solutions of the YBMF x were 0.2 M, and they were obtained as precursors for film deposition. The films were deposited by spin coating onto the quartz substrates at a

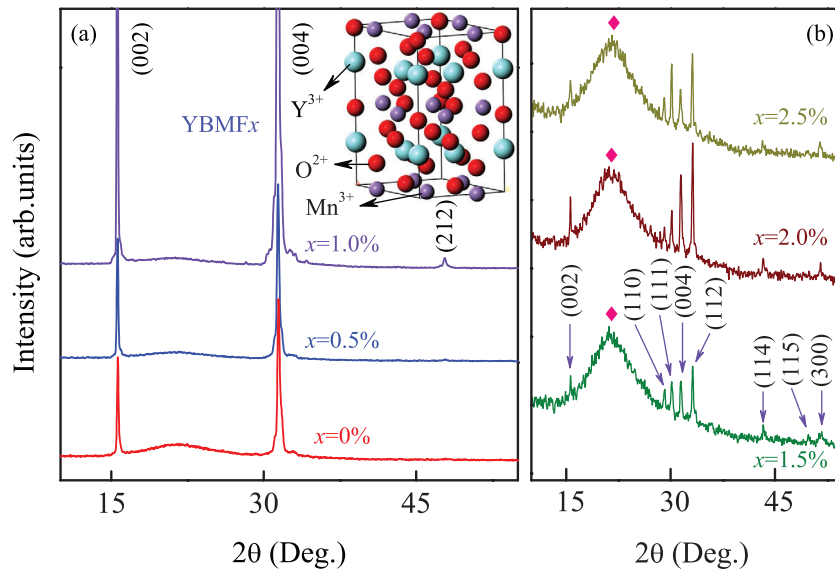


Figure 1. The XRD patterns of (a) highly c -axis-oriented YBMF x ($0 \leq x \leq 1.0\%$) films, and (b) not preferred YBMF x ($1.5\% \leq x \leq 2.5\%$) films. Note that the diamond indicates the observed trace of the quartz substrate. The inset shows the schematic illustrations of the h -YMO unit cell.

speed of 4000 rpm for 20 s. Each layer of the films was dried at 300 °C for 300 s and then pyrolyzed at 500 °C for 300 s to remove residual organic compounds, followed by annealing at 900 °C for 200 s by a rapid thermal annealing procedure. The spin-coating and annealing-treatment procedures were repeated eight times to obtain the desired thickness.

2.2. Microstructure, morphology, XPS, ferroelectric and optical characterizations of YBMF x films

The crystalline structure of YBMF x films on quartz substrates were analyzed by x-ray diffraction (XRD: Bruker D8 Advance diffractometer) using Cu $K\alpha$ radiation ($\lambda = 0.1542$ nm) at room temperature (RT). The surface morphology of films was investigated by atomic force microscopy (AFM: digital instruments icon, Bruker) with the ScanAsyst modes. The cross-section microstructure of films were characterized using a scanning electron microscope (SEM: S-3000N, Philips XL30FEG). The elemental mapping was obtained by an energy dispersive x-ray spectroscopy (EDS) detector. X-ray photoelectron spectroscopy (XPS) experiments were carried out on a RBD upgraded PHI-5000C ESCA system (Perkin-Elmer) with Mg $K\alpha$ radiation ($h\nu = 1253.6$ eV). Platinum (Pt) dots with the diameter of about 0.2 mm deposited by a sputtering technique using a shadow mask are used as the top electrodes for electrical measurements, while the Pt layer served as a bottom electrode. The hysteresis loops of the Pt/YBMF x/n^+ -Si capacitor were measured using a ferroelectric test system (Precision Premier II: Radiant Technologies, Inc.). The normal-incident transmittance spectra of the YBMF x films on quartz substrates were recorded by a double beam ultraviolet-infrared spectrophotometer (PerkinElmer Lambda 950) at the photon energy from 0.5 to 6.5 eV (190–2650 nm) with a spectral resolution of 2 nm. The films were mounted into a closed cycle refrigerator system (Janis SHI-4-1), where the temperature can be varied from 10 to 300 K.

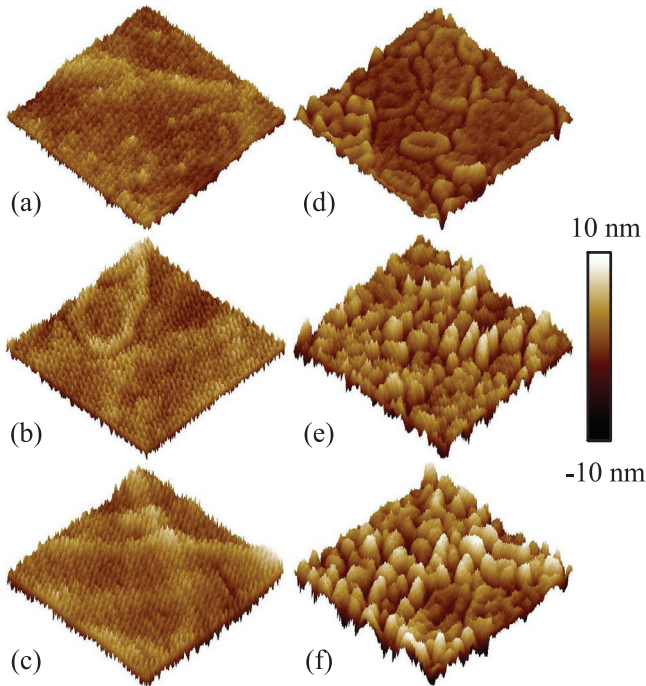
3. Results and discussion

3.1. Structural and surface analysis

The XRD patterns of YBMF x ($0 \leq x \leq 2.5\%$) films prepared on quartz substrates are shown in figure 1, and fitting results are shown in table 1. As can be seen, all films exhibit a single phase with the hexagonal structure (space group $P6_3cm$ shown in the inset of figure 1, JCPDS card No.25-1079) and no impurity phase was observed. Obviously, there are the HCO series and the NPO series. The YMO, YBMF0.5% and YBMF1.0% films taken as the HCO series show the conspicuous (001) diffraction peaks, indicating the growth of highly c -axis-oriented film. On the other hand, with the amount of Fe and Bi, some other hexagonal crystal peaks (110), (111), (112), (114), (212) and (300) can also be detected. The highly c -axis-oriented YMO without no doping is likely to be related to the choice of the solvent and solution. Kitahata *et al* reported that the crystal orientation of sol-gel YMO film on the quartz substrate is not a preferred orientation [33]. The present solvent and solution is different from their report. Thus, the choice of the solvent and solution is possibly an important fact for obtaining the preferred orientation. The conspicuous (001) diffraction peaks of the YBMF0.5% and YBMF1.0% films can be mainly attributed to Bi doping, which further contributed to c -axis-orientation [28]. Note that a smaller amount of Fe and Bi co-doping further leads to highly c -axis-oriented growth than that from the previous report [28]. It contributed to weakening the significant Bi_2O_3 surface layer due to the Bi doped concentration being much less than 5% [28]. The several hexagonal crystal peaks for the YBMF x ($1.5\% \leq x \leq 2.5\%$) films (as the NPO series) indicate that the larger co-doping concentration has a great influence on the property of c -axis-oriented h -YMO. The choice of solvent and solution, and the Fe and Bi co-doping realized the modulation of h -YMO films, especially, for the significant modulation of crystal orientation.

Table 1. The position and FWHM of the (002), (004) and (1 1 2) diffraction peaks for the YBMF x ($0 \leq x \leq 2.5\%$) films determined from the XRD patterns.

Samples	Peak position/ $^{\circ}$			FWHM/ $^{\circ}$			$d_{hkl}/\text{\AA}$			Grain size/nm		
	(002)	(004)	(1 1 2)	(002)	(004)	(1 1 2)	(002)	(004)	(1 1 2)	(002)	(004)	(1 1 2)
YMO	15.64	31.47	—	0.18	0.30	—	5.66	2.84	—	49.79	30.41	—
YBMF0.5%	15.61	31.41	—	0.15	0.29	—	5.67	2.85	—	59.07	32.05	—
YBMF1.0%	15.59	31.38	—	0.13	0.23	—	5.68	2.85	—	68.66	40.29	—
YBMF1.5%	15.63	31.48	33.17	0.16	0.31	0.25	5.66	2.84	2.70	58.90	23.91	36.82
YBMF2.0%	15.61	31.48	33.16	0.14	0.29	0.24	5.67	2.84	2.70	63.67	31.60	39.20
YBMF2.5%	15.62	31.38	33.12	0.25	0.33	0.24	5.67	2.84	2.70	58.83	27.76	38.85

**Figure 2.** Three-dimensional AFM images of (a) YMO, (b) YBMF0.5%, (c) YBMF1.0%, (d) YBMF1.5%, (e) YBMF2.0%, and (f) YBMF2.5%, respectively. Note that the scale height is 20 nm and the measured area is $1 \times 1 \mu\text{m}^2$.

The three-dimensional AFM images of the YBMF x ($0 \leq x \leq 2.5\%$) films prepared on quartz substrates are shown in figure 2. The co-doping of Bi and Fe has a significant modulation of surface morphology. For the NPO series, there is greater ups and downs of morphology with increasing concentration than the regular and flatter surface morphology of HCO series. The root-mean-square roughness values are estimated to be 1.71, 1.81, 2.11, 2.05, 2.97, and 3.50 nm for $x = 0, 0.5\%, 1.0\%, 1.5\%, 2.0\%$, and 2.5% , respectively. Considering the analysis of XRD patterns and AFM images, the co-doping of Bi and Fe not only modulates the surface morphology, but also plays an important role in the crystal orientation. A layer of film was taken as the seed crystal of subsequent film in the process of film preparation, which has an effect on the film growth by the surface morphology. It can well explain the consistency of the results derived from the XRD and AFM. The modulation of Fe and Bi co-doping on the crystal lattice and morphology of h -YMO film provides

the important reference value for the growth of other hexagonal rare earth manganite films.

The surface and cross-sectional SEM images are shown in figure 3. It is found that grain boundaries gradually appear with increasing concentrations. The higher c -axis-oriented h -YBMF x film can cause the significant crack from figure 3(c). However, several hexagonal crystalline orientations suppress a part of the crack and increase more pinholes for the NPO series. Besides, it can be concluded from the cross-sectional pictures that the films are compacted and the thicknesses of the h -YBMF x films are 234, 249, 228, 231, 234, and 261 nm for $x = 0, 0.5\%, 1.0\%, 1.5\%, 2.0\%$, and 2.5% , respectively.

In order to confirm the homogeneous distribution of Fe and Bi, the EDS mappings were tested. The EDS mapping can demonstrate where the Bi and Fe located on the material surface. The mappings of 2.5% doped film are shown in figure 4. From figure 4, it indicates the homogeneous distribution of elements.

3.2. XPS analysis and ferroelectric properties

In order to confirm elements and valences, YBMF x crystal were studied by XPS measurements. The XPS spectra of YMnO_3 are shown in figures 5(a)–(c). The binding energy peaks of Y 3 d , Mn 2 p , and O 1 s have been indexed in figure 5(a). From the inset of figure 5(a), two fitting peak positions of Mn 2 p are 653.7 eV ($2P_{1/2}$) and 642.2 eV ($2P_{3/2}$), respectively. The results are in agreement with the recent report [34]. It indicates that the valence of manganese ions is +3 for YMnO_3 . From figures 5(b) and (c), the fitting peak positions of O 1 s level and Y 3 d level are 529.3 eV and 156.9 eV, respectively. It is in agreement with Kochur's report [35]. The energy position of A component is about 531.4 eV due to typical adsorbed oxygen. The influence of Fe and Bi co-doping on the Mn 2 p level is shown in figure 5(d). The linear fitting results indicate that peak positions of Mn 2 p level move to higher energy with increasing concentration.

The polarization-electric field (P - E) hysteresis loops of the Pt/YBMF x/n^+ -Si capacitor were measured at room temperature and $f = 1$ kHz. The P - E hysteresis loops of the Pt/ YMnO_3/n^+ -Si capacitor is shown in figure 5(e). The remanent polarization ($2P_r$) and the coercive field ($2E_c$) are two important characteristics of ferroelectricity. From figures 5(f) and (g), there is an optimal doping concentration of $x = 1.5\%$

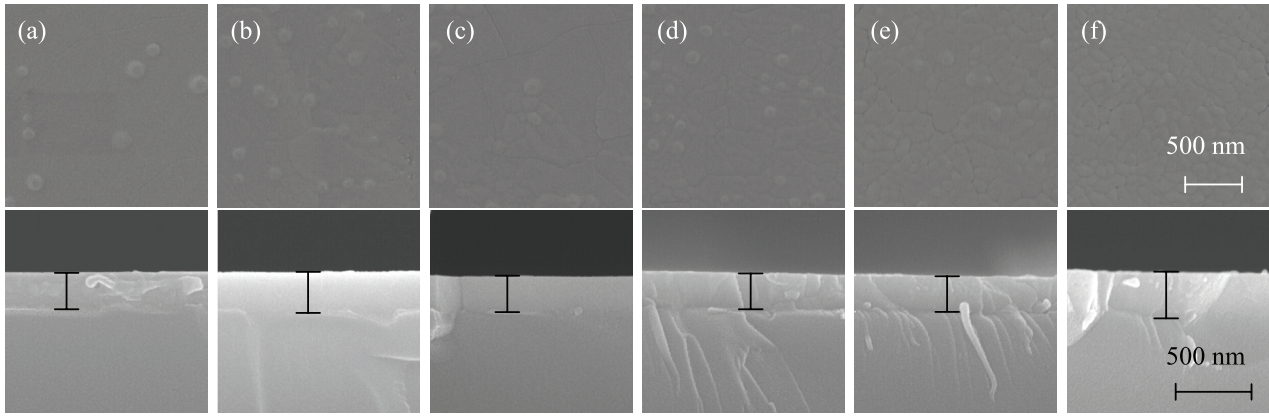


Figure 3. The plane-view and the corresponding cross-sectional SEM images of (a) YMO, (b) YBMF0.5%, (c) YBMF1.0%, (d) YBMF1.5%, (e) YBMF2.0%, and (f) YBMF2.5% films on quartz substrates, respectively.

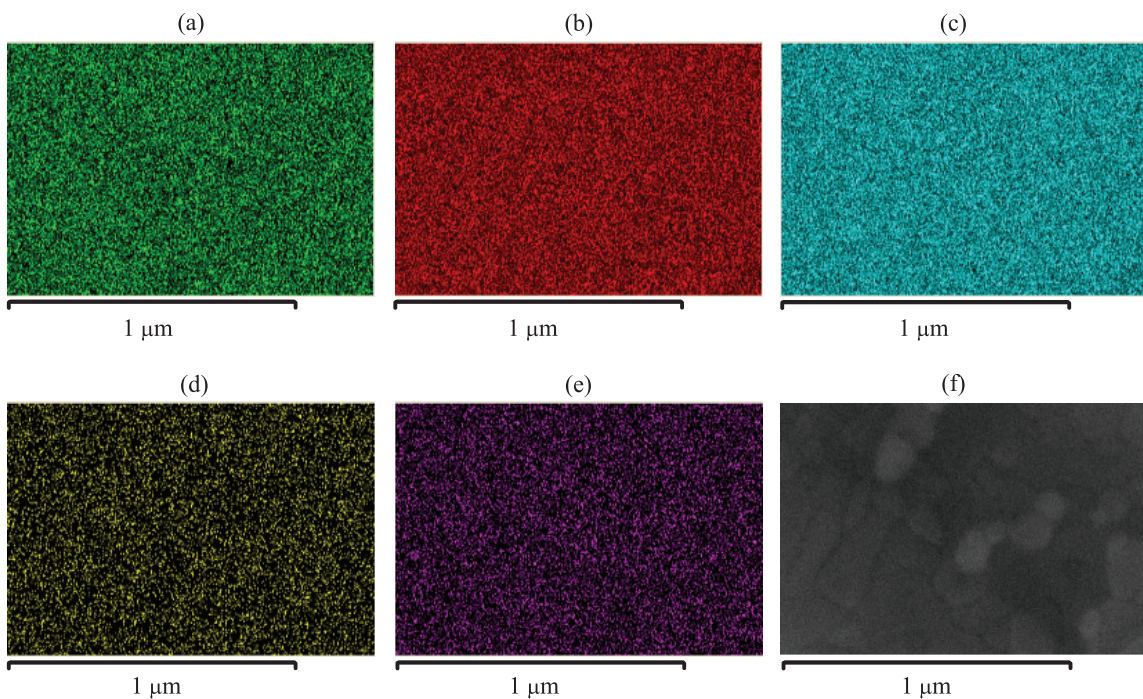


Figure 4. The EDS mappings and corresponding scanning area of 2.5% doped film: (a) Mn, (b) O, (c) Y, (d) Fe, (e) Bi, and (f) the scanning area.

for the YBMF x ($0 \leq x \leq 2.5\%$) films by taking the shapes of P - E loops and the values of $2P_r$ and $2E_c$ into consideration. It means that the higher c -axis-orientation for YBMF x films can not bring out better ferroelectric behaviour due to some crack. However, several hexagonal crystal orientations suppress a part of crack at the present YBMF x films by the analysis of SEM patterns. Thus, controlling crack is more significant to improve ferroelectric properties for the YBMF x films. Although the larger leakage currents appear for the present sol-gel films, the ferroelectric properties of samples superior to recent report of h -YMO films [36]. By the XPS analysis and ferroelectric properties, the h -YMO film was further confirmed.

3.3. Concentration and temperature dependent double energy gaps

3.3.1. Confirmation of double energy gaps. The optical transmittance spectra of the YBMF x ($0 \leq x \leq 2.5\%$) films on quartz substrates measured at RT were shown in figure 6(a). It is very similar to the transmittance spectra of hexagonal TbMnO_3 [22]. The transmittance of the YBMF x films approach about 50–70% at the wavelength from 950 to 2000 nm. Moreover, the optical transmittance spectra shows two absorption edges, corresponding to two gaps, respectively. The smaller gap is often considered as the band gap (E_{g1}), and the other is the subband gap (E_{g2}). From figure 6(a), the valleys of the arrows

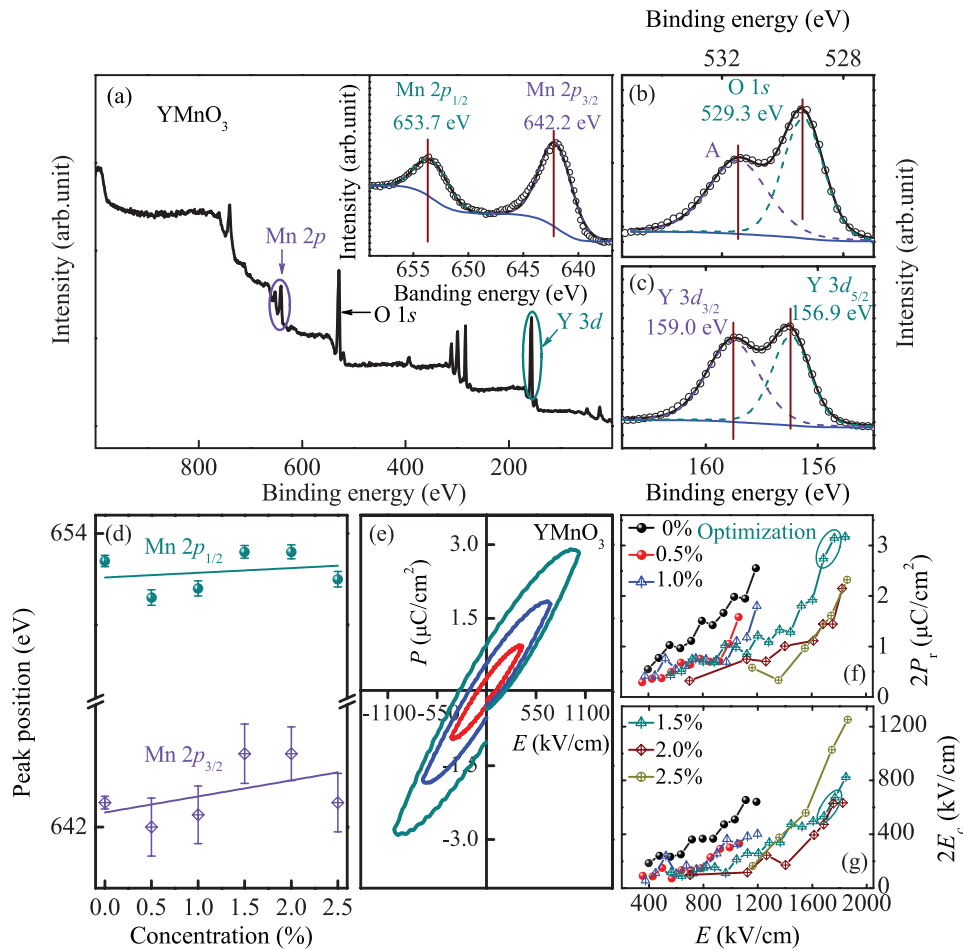


Figure 5. (a) XPS spectra of YMO film. The inset is an enlargement of the Mn 2p region. (b) and (c) correspond to the enlargement of the O 1s region and Y 3d region, respectively. (d) Position of the Mn 2p peak of the YBMF x ($0 \leq x \leq 0.025$) films as a function of co-doping concentration. (e) P - E hysteresis loop of the YMO film as a function of the electric field measured at 1 kHz and room temperature. (f) $2P_r$ and (g) $2E_c$ of the YBMF x films.

correspond to the optical energy gap absorptions of the E_{g1} and E_{g2} , respectively.

The optical band gap, E_{OBG} is deduced by Tauc's relation $(\alpha h\nu)^n = A(h\nu - E_{OBG})$ [37, 38]. Here, α denotes the absorption coefficient obtained by the relation $\alpha = -d^{-1} \ln T$. d is the film thickness, and T is the transmittance of film. The nature of the band gap is identified by the exponent n and an intercept of the $(\alpha h\nu)^n$ plot with photon energy $h\nu$. h is Planck's constant, and ν is the photon frequency. Picozzi *et al* identified that $YMnO_3$ is an indirect band gap semiconductor by the first-principles calculations [39]. Moreover, Wang *et al* also use the mode of the indirect bandgap semiconductor for estimating the band gap of $YMnO_3$, majorly with hexagonal structure [40]. Therefore, in order to study the energy band gaps of YBMF x films, the band gap can be estimated from the plots of $(\alpha h\nu)^{1/2}$ versus $h\nu$ using Tauc's relation [41], as shown in figure 6(b).

From figure 6(b), it shows the band gap of YMO is about 1.25 eV, which is in agreement with about 1.2 eV [40, 42], less than about 1.5 eV [8, 14, 15], and larger than about 0.5 eV [39]. It is possibly related to the release of excessive stress under the condition of high temperature preparation [40]. However, considering the influence of the hexagonal crystal

field on h -YMO, Mn 3d energy levels split into three sub-levels, hybridized with O 2p energy levels in a certain degree, respectively. Therefore, there should be two interband transition. Moreover, two interband transition energies correspond to about 1.7 eV and 2.3 eV, respectively [22, 43]. Recently, Kumar *et al* reported the result of the valence band structure of h -YMO [9]. Three peaks appear at 4.1, 5.9 and 7.1 eV, respectively. According to Kumar's level assignment, the E_{g1} and E_{g2} could be estimated to be about 1.8 eV and 3 eV, respectively. From figure 6(b), the E_{g2} of h -YMO is about 3.3 eV, which is closer to 3 eV. In general, the experimental value is higher than the theoretical value due to the huge stress and imperfect crystallinity for the band gap of the film prepared by the sol-gel technique [44, 45]. However, the huge stress and imperfect crystallinity significantly promotes the expansion of the sub-band gap for sol-gel h -YMO film. According to the analysis of the transmittance, the possible simplified diagram of energy bands can be derived, as shown in figure 6(c), where the Fermi level (E_F) and key hybrid forms are referred to in [22].

3.3.2. Concentration and temperature dependent E_{g1} . In order to further explore concentration and temperature dependent double energy gaps, variable temperature transmission

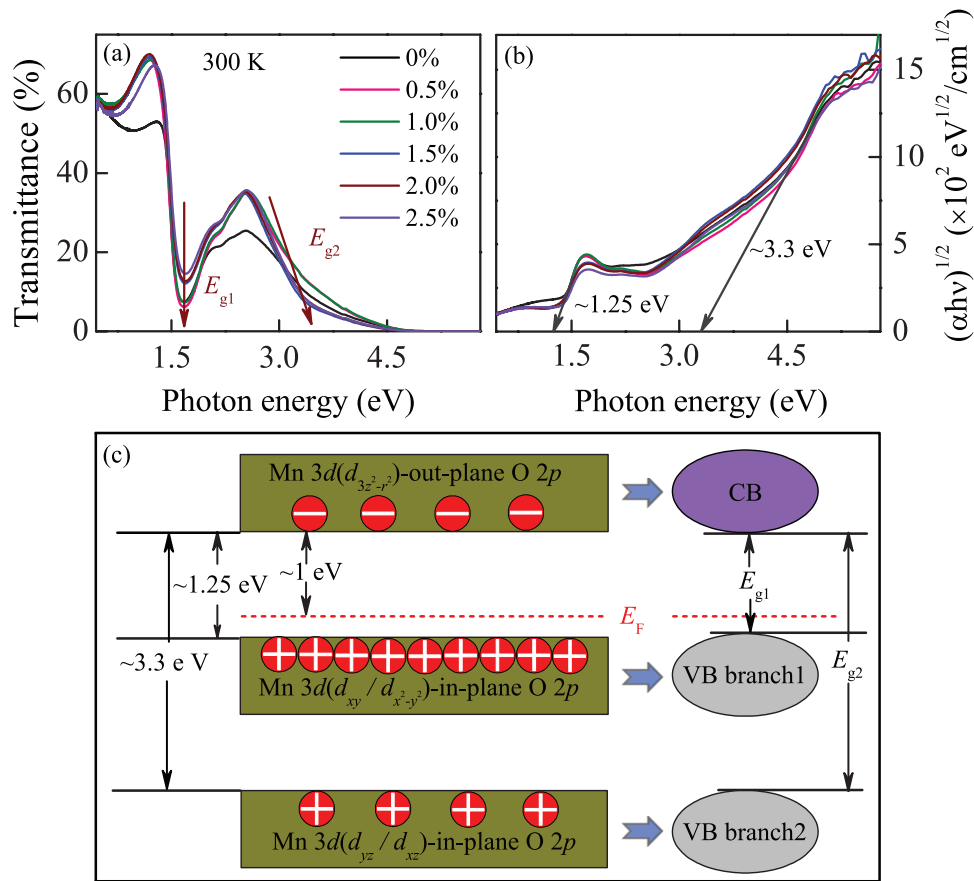


Figure 6. (a) The transmittance spectra of the YBMF x ($0 \leq x \leq 2.5\%$) films at RT. The valleys of the arrows correspond to the optical transition of the E_{g1} and E_{g2} , respectively. (b) Plots of $(\alpha h\nu)^{1/2}$ versus the photon energy for the estimation of indirect band gap energies from the YBMF x ($0 \leq x \leq 2.5\%$) films. The arrows correspond to E_{g1} (~ 1.25 eV) and E_{g2} (~ 3.3 eV) for h -YMO, respectively. (c) The simplified three-band system of the YMnO₃ film, Fermi level and key hybrid forms referred to in [22] (not taking into account the hybridization related to O s levels, Y sp/d levels, and Mn sp levels).

Table 2. The E_{g1} of the YBMF x ($0 \leq x \leq 2.5\%$) films by the linear fitting of the determined E_{g1} absorption edge.

Samples	E_{g1} (eV)					
	10K	75K	145K	200K	250K	300K
YMO	1.430	1.393	1.367	1.335	1.320	1.271
YBMF0.5%	1.407	1.371	1.351	1.327	1.311	1.260
YBMF1.0%	1.393	1.362	1.349	1.328	1.311	1.274
YBMF1.5%	1.361	1.337	1.303	1.286	1.262	1.237
YBMF2.0%	1.315	1.306	1.297	1.287	1.267	1.242
YBMF2.5%	1.409	1.369	1.339	1.309	1.274	1.254

spectra were investigated. The results of large absorption edge E_{g1} by the linear fitting are shown in table 2 and figure 7(a). The shrinkage of E_{g1} with doping concentration from 1.0% to 1.5% was conformed in figure 7(a). It can be attributed to the change of crystal orientation due to the co-doping. Nevertheless, the change of crystal orientation cannot explain the variation E_{g1} with increasing concentration for the HCO series and the NPO series, respectively.

From figure 7(a), above 200 K, the E_{g1} for the HCO series firstly becomes narrow with increasing doping concentration.

Then, the E_{g1} for the HCO series expands. (There are similar fitting results for YBMF0.5% and YBMF1.0% at 200 K due to the nonsignificant difference.) Note that the E_{g1} for the NPO series monotonously increases with increasing doping concentration above 200 K.

According to the XRD analysis, the c -axis-orientational peak monotonously enhances with increasing doping concentration for the HCO series. From table 1, the improvement of crystallinity of the HCO series indicates that the co-doping plays a certain positive effect and possibly repairs some defects. Note that doping itself can destroy the lattice perfection to an extent. Thus, the two effects compete with each other. When doping concentration is less than and equal to 0.5%, the destruction of the lattice perfection is stronger than the remedying of the defect, which leads to the decreasing of E_{g1} . When doping concentration reaches 1.0%, however, the destruction of the lattice perfection is weaker than the remedying of defects, leading to the expansion of E_{g1} . In fact, the similar fitting results for YBMF0.5% and YBMF1.0% at 200 K indicated that the competition between two effects is almost balanced.

For the NPO series, both the significant improvement of crystallinity and highly c -axis-orientation disappear, indicating non-significant repair-deficiency or relatively serious

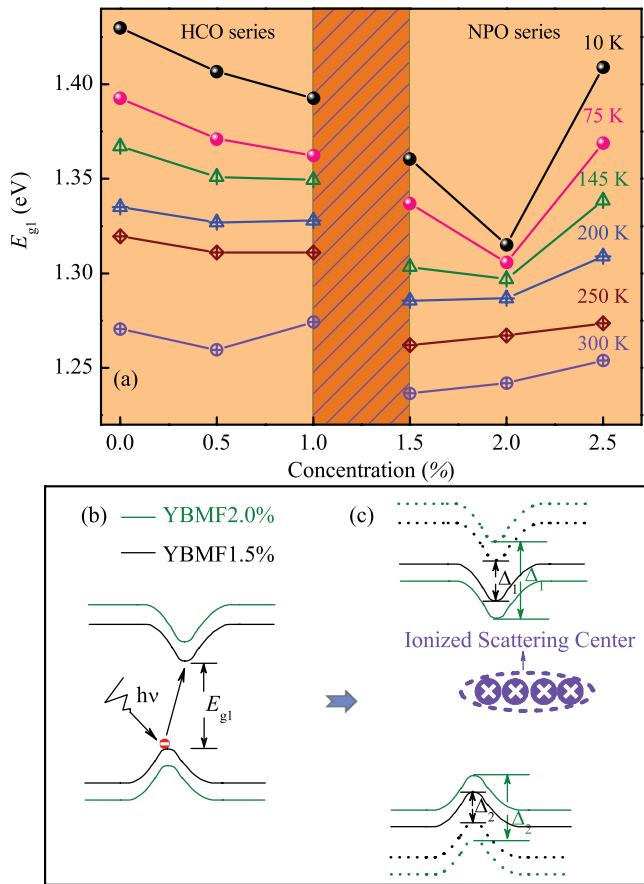


Figure 7. (a) Temperature dependencies of E_{g1} : the shadow region is a transition region from preferred orientation to no preferred orientation. Ionized impurity scattering can explain the change of composition dependence of E_{g1} with doping concentration from 1.5% to 2.0% below 145 K; (b) the expansion of E_{g1} with doping concentration above 200 K; (c) the shrinkage of E_{g1} with doping concentration below 145 K. The energy band structure of dotted lines corresponds to the ideal case without considering ionized impurity scattering. The solid line corresponds to the actual case. Due to strong ionized impurity scattering, additional energy $\Delta_1 + \Delta_2$ is the probable reason for the change of composition dependence.

lattice defect. However, the relatively serious lattice defect leads to the expansion of E_{g1} . It is different from the shrinkage of E_{g1} due to the effect of lattice defect with the doping concentration from 0 to 0.5%. The expansion of E_{g1} for the NPO series could not simply be attributed to the strong competition of two effects. As we know, the expansion of band gap can be found in some doped compound semiconductors, for example, $Ga_{1-x}In_xN$ ($E_g = 0.7$ eV to 3.4 eV), $Ga_{1-x}Al_xN$ ($E_g = 3.4$ eV to 6.2 eV) and $Zn_{1-x}Be_xO$ ($E_g = 3.3$ eV to 10.6 eV) [46–48]. For NPO series, the concentration dependence of E_{g1} above 200 K is possibly attributed to the similar expansion (SE) at least in part due to the band gap of $YMnO_3$ (~ 1.5 eV) smaller than $BiFeO_3$ (~ 2.7 eV) [8]. However, it requires more thorough research.

Below 145 K, the tendency of E_{g1} is different from that above 200 K. The E_{g1} monotonously decreases for the HCO series. However, the E_{g1} for the NPO series firstly decreases. Then it increases with increasing doping concentration. As we know, there are different scattering mechanisms at different

temperature. Several scattering mechanisms have influences on the valence electrons of optical band gap absorption and transition [49]. For example, the lattice thermal vibration or phonon scattering is the main scattering mechanism at higher temperatures. It contributes to the fact that the valence electrons are more easily out of valence bonds and enter the conduction band as the free electrons. In fact, the process can be seen as the valence electron interacting with the phonon. It is referred to as the energy absorption and possible momentum exchange.

There are often three main scattering mechanisms, for the present films, including surface scattering, ionized impurity scattering and the lattice thermal vibration [50]. Surface scattering mainly depends on the roughness on the surface. However, the temperature variation has little influence on the surface roughness and can be ignored. In addition, the lattice thermal vibration become weaker below 145 K. The ionized impurity scattering possibly becomes a main factor. The lattice shrinkage often leads to the shorter distance between the ionized impurity center and the surrounding valence electrons at the lower temperatures. It will enhance the Coulomb force and improve the ionized impurity scattering. The valence electrons near the ionized impurity center possibly get a part of the energy and transfer a part of the momentum by stronger ionized impurity scattering below 145 K. It explains the shrinkage of E_{g1} with doping concentration from 0.5% to 1.0% below 145 K well. Similarly, the strong ionized impurity scattering also explains the shrinkage of E_{g1} with doping concentration from 1.5% to 2.0% below 145 K, as shown in figures 7(b) and (c).

When doping concentration approaches 2.5%, however, the shrinkage of E_{g1} disappears below 145 K. It can be attributed to inadequate ionization of impurities due to the higher doping concentration. As we know, the incomplete ionization of impurity is most significant in the condition of high doping levels and at low temperatures [51]. The ionization degree of impurity decreased with increasing doping concentration especially at lower temperatures [52, 53]. Thus, the inadequate ionization of impurities can well explain the expansion of E_{g1} with the doping concentration from 2.0% to 2.5%. Moreover, the shrinkage of E_{g1} due to the ionized impurity scattering should be relatively weaker than the SE of E_{g1} . At the lower temperature, besides of lattice thermal vibration, the ionized impurity scattering should be considered [54]. It explains different dependencies of E_{g1} below 145 K and above 200 K well.

3.3.3. Concentration and temperature dependent E_{g2} . Concentration and dependent E_{g2} is shown in figure 8(a). Realizing the significant difference of line slopes, there are roughly two tendencies of E_{g2} at the lower temperature range I and the higher temperature range II. Moreover, the critical temperature point (T_c) of the two temperature ranges is near 100 K. At the higher temperatures, the E_{g2} firstly increases with increasing composition. Then, it decreases with increasing composition. However, at the lower temperatures, the trends of E_{g2} become more complicated. The T_c (~ 100 K) is possibly related to the antiferromagnetic phase transformation. Note that the T_c is closer to the Néel temperature T_N (~ 70 K)

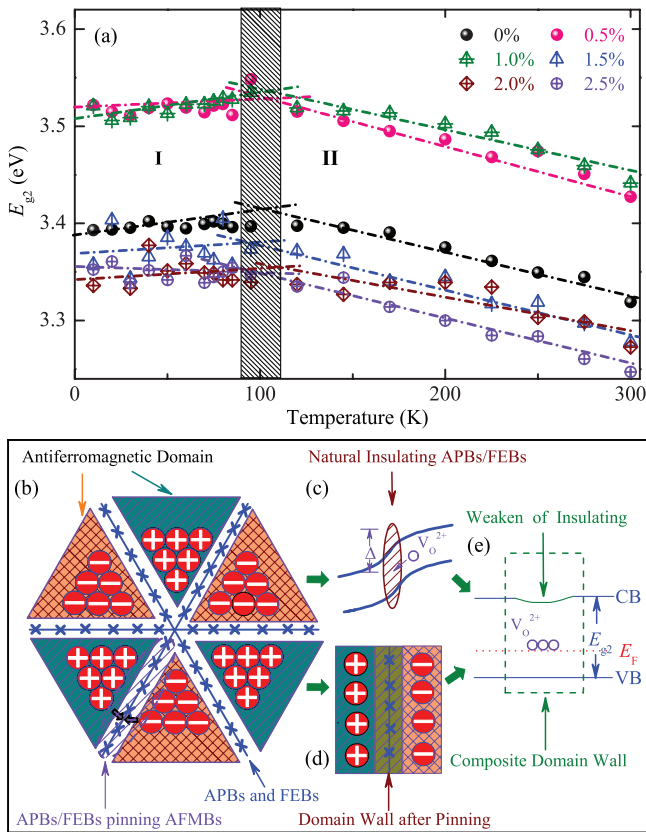


Figure 8. (a) Temperature dependent E_{g2} : there are roughly two tendencies of E_{g2} at the lower temperature range I and the higher temperature range II due to the significant difference of slopes. The critical temperature point of two ranges I and II is about 100 K. The pinning effect explains the abnormal shrinkage of E_{g2} below 100 K for all samples. (b) When magnetic order occurs at low temperatures, the interlocked APBs and FEBS will pin AFMBs for a vortex ferroelectric domain. The charge polarity indicates the polarity of ferroelectric domain. (c) The interlocked APBs and FEBS are natural insulating. Δ indicates a lower potential energy barrier due to the polarity of the ferroelectric domain. Discrete oxygen vacancy migrate to APBs/FEBS. (d) The composite domain wall is formed due to the pinning effect. (e) Magnetic-ordering-dependent electronic excitation and the pinning effect can accelerate the accumulation of discrete oxygen vacancies at composite domain walls. The decreasing insulation of the composite domain wall corresponds to the shrinkage of E_{g2} .

[12, 13]. As we know, anomalous change of permittivity or magnetic permeability often occurs near the phase transition temperature. According to Katsufuji’s model [21], the change of the antiferromagnetic ordering pattern can induce an abnormality via the change of E_g , based on the formula $\varepsilon = (1/E_g)^2$. The E_{g1} and E_{g2} of YMO could be attributed to the gaps between two hybridized bands by the optical conductivity spectra and theoretical calculation [22]. Mn^{3+} ‘trimerization’ antiferromagnetic structure could cause the tilting of the Mn-O triangular bipyramid cage and the bulking of the Mn-O plane [21, 55, 56], which has some effect on E_{g1} and E_{g2} at the process of antiferromagnetic phase transformation. However, from figure 7(a), there is no significant anomaly for temperature dependent E_{g1} for all samples. It is in agreement with the fact that magnetic ordering does not affect the

charge-transfer excitation between the Mn state and the apical oxygen state based on Katsufuji’s model. Interestingly, a significant anomaly appears for temperature dependent E_{g2} . From figure 8(a), there is an abnormal shrinkage of E_{g2} below ~ 100 K. The magnetic-ordering-dependent electronic excitation has a significant influence on the E_{g2} of YMO by the modulation of the hybridization between in-plane O 2p orbitals and the associated Mn E_{1g} orbitals. Thus, considering the above modulation, the T_c (~ 100 K) is possibly related to antiferromagnetic phase transformation.

Recently, Harunsani *et al* reported that there is spontaneous formation of circular and vortex ferroelectric domain structure in YMO prepared by the low-temperature hydrothermal method [57]. They pointed out that the structural phase transition is not the only factor for the occurrence of the annular and vortex domains. A solution-mediated condition provides a distinct environment for crystal growth. Thus, there are possible spontaneous formation of vortex ferroelectric domain structure in the present YMO film due to adopting the environment of solution. As we know, vortex ferroelectric domain results from mutual locking of structural antiphase domain boundaries (APBs) and ferroelectric domain boundaries (FEBS) [8]. The structural APBs are naturally antiferromagnetic domain boundaries. When magnetic order occurs at low temperatures, the interlocked walls tend to pin antiferromagnetic domain boundaries (AFMBs). It means that the antiferromagnetic effect possibly makes relaxation phenomenon occur near and above the antiferromagnetic phase transformation temperature. In addition, there are often some oxygen vacancy defects for sol-gel films. Oxygen vacancies often have the ability of pinning domain boundaries [5, 58]. Moreover, Maeda *et al* reported that electromagnetic coupling effect still existed at about 120 K in *h*-YMO, which is higher than the Néel temperature [59]. It means that antiferromagnetic effect possibly exists above the Néel temperature. It can explain that the T_c of *h*-YMO near 100 K is higher than T_N (~ 70 K). Thus, T_c near about 100 K is possibly related to the relaxation of antiferromagnetic phase transformation. However, the T_c was possibly nonsignificant or unobserved in traditional magnetic transition measurements. Except for the present optical method and a report, there are no more methods and reports to confirm the critical temperature due to our limited knowledge. The critical point T_c was indeed observed in the present work. It indicates that the variable temperature transmittance provides a possible method to observe nonsignificant or unobserved phenomenon of traditional magnetic transition measurements.

In order to explain the abnormal shrinkage of E_{g2} below 100 K, the pinning effect of the composite domain wall was proposed, as shown in figures 8(b)–(e). The discrete oxygen vacancies can migrate in the crystal lattice by applying the electric field due to their low activation energy compared to the ordered ones at the composite domain wall [60]. Magnetic-ordering-dependent electronic excitation and the pinning effect might accelerate the accumulation of discrete oxygen vacancies at composite domain walls. It can lead to the abnormal shrinkage of E_{g2} below 100 K. It is in agreement with that domain walls in oxygen deficiency $YMnO_3$

are reported to exhibit significantly enhanced conductance [4, 60]. Although the abnormal shrinkage of E_{g2} below 100 K can be explained, it needs much more thorough research.

As we know, the Fe-doping can result in the improvement of the T_N [29, 61]. Nevertheless, the T_C of YBMF x ($0.5\% \leq x \leq 2.5\%$) is still near 100 K. It means that the present Fe-doping has a relatively small impact on the T_C due to the relaxation of antiferromagnetic phase transformation. More concrete influence of relaxation of antiferromagnetic phase transformation is still an open question due to the present limit experiments.

4. Summary

In this work, the highly c -axis-orientated h -YMO polycrystal film and the Fe and Bi co-doped h -YMO films were successfully prepared by the sol-gel technique. The choice of solvent and solution, and the Fe and Bi co-doping realized the modulation of h -YMO films, especially, for the significant modulation of crystal orientation. A smaller amount of Bi with Fe co-doping further contributes to higher c -axis-oriented growth, while a larger amount of co-doping leads to no preferred orientation. The results of AFM measurement reveals that Fe and Bi co-doping can significantly modulate surface morphology. The results of XPS confirmed that manganese ions show a valence of +3 in $Y\text{MnO}_3$ film. The peak positions of the Mn $2p$ level move to higher energy with increasing concentration. There is an optimal doping concentration of $x = 1.5\%$ for the ferroelectric properties of the YBMF x ($0 \leq x \leq 2.5\%$) films. By the XPS analysis and ferroelectric properties, the h -YMO film was further confirmed. The double energy gaps (~ 1.25 eV and 3.3 eV) corresponded to significant absorption edges, the band gap (E_{g1}) and sub-band gap (E_{g2}), respectively. The ionized impurity scattering explained different dependency of E_{g1} below 145 K. The T_C (~ 100 K) of E_{g2} can be attributed to the relaxation of antiferromagnetic phase transformation. The abnormal shrinkage of E_{g2} below 100 K can be explained by the pinning effect of composite domain walls and the accumulation of discrete oxygen vacancies at composite domain walls. The E_{g1} meets Katsufuji's model, but E_{g2} does not meet Katsufuji's model. The relaxation of antiferromagnetic phase transformation possibly has a significant influence on the E_{g2} .

Acknowledgments

This work was financially supported by Major State Basic Research Development Program of China (Grant No. 2013CB922300), the Natural Science Foundation of China (Grant Nos. 11374097, 61376129, and 61504156), Projects of Science and Technology Commission of Shanghai Municipality (Grant Nos. 15JC1401600 and 14XD1401500), and the Program for Professor of Special Appointment (Eastern Scholar) at Shanghai Institutions of Higher Learning.

References

- [1] Eerenstein W, Mathur N D and Scott J F 2006 *Nature* **442** 759
- [2] Wu H, Yuan J, Peng T, Pan Y, Han T, Shen K, Zhao B R and Liu C 2009 *J. Phys. D: Appl. Phys.* **42** 185302
- [3] Tokura Y and Seki S 2010 *Adv. Mater.* **22** 1554
- [4] Jiang N and Zhang X 2015 *J. Phys. D: Appl. Phys.* **48** 435503
- [5] Du Y, Wang X L, Chen D P, Yu Y X, Hao W C, Cheng Z X and Dou S X 2013 *Phys. Chem. Chem. Phys.* **15** 20010
- [6] Bogusz A et al 2016 *Appl. Phys. Lett.* **108** 052103
- [7] Tian L, Wang Y M, Ge B H, Zhang X Q and Zhang Z H 2015 *Appl. Phys. Lett.* **106** 112903
- [8] Choi T, Horibe Y, Yi H T, Choi Y J, Wu W D and Cheong S-W 2010 *Nat. Mater.* **9** 253
- [9] Kumar M, Choudhary R J and Phase D M 2013 *Appl. Phys. Lett.* **102** 182902
- [10] Thomson R I, Chatterji T, Howard C J, Palstra T T M and Carpenter M A 2014 *J. Phys.: Condens. Matter* **26** 045901
- [11] Kumar M, Choudhary R J and Phase D M 2015 *J. Phys. D: Appl. Phys.* **48** 125003
- [12] van Aken B B, Palstra T T M, Filippetti A and Spaldin N A 2004 *Nat. Mater.* **3** 164
- [13] Singh A K, Patnaik S, Kaushik S D and Sirugiri V 2010 *Phys. Rev. B* **81** 184406
- [14] Kalashnikova A M and Pisarev R V 2003 *J. Exp. Theor. Phys. Lett.* **78** 143
- [15] Schmidt-Grund R, Richter S, Ebbinghaus S G, Lorenz M, Bundesmann C and Grundmann M 2014 *RSC Adv.* **4** 33549
- [16] Xiao H 2012 *Introduction to Semiconductor Manufacturing Technology* (Washington, DC: SPIE)
- [17] Sze S M and Ng K K 2007 *Physics of Semiconductor Devices* (Hoboken, NJ: Wiley)
- [18] Ito D, Fujimura N, Yoshimura T and Ito T 2003 *J. Appl. Phys.* **94** 4036
- [19] Ghosh G 1996 *J. Appl. Phys.* **79** 9388
- [20] Yoo H G and Fauchet P M 2008 *Phys. Rev. B* **77** 115355
- [21] Katsufuji T, Mori S, Masaki M, Moritomo Y, Yamamoto N and Takagi H 2001 *Phys. Rev. B* **64** 104419
- [22] Choi W S et al 2008 *Phys. Rev. B* **77** 045137
- [23] Shigemitsu N, Sakata H, Ito D, Yoshimura T, Asida A and Fujimura N 2004 *Japan. J. Appl. Phys.* **43** 6613
- [24] Chye Y, Liu T, Li D, Lee K, Lederman D and Myers T H 2006 *Appl. Phys. Lett.* **88** 132903
- [25] Tomczyk M, Senos A M, Vilarinho P M and Reaney I M 2012 *Scr. Mater.* **66** 288
- [26] Tomczyk M, Senos A M O R, Reaney I M and Vilarinho P M 2012 *Scr. Mater.* **67** 427
- [27] Rokuta E, Hotta Y, Tabata H, Kobayashi H and Kawai T 2000 *J. Appl. Phys.* **88** 6598
- [28] Choi T and Lee J 2004 *Appl. Phys. Lett.* **84** 5043
- [29] Han T-C, Wu P-J and Shih Y-L 2012 *J. Appl. Phys.* **111** 07B511
- [30] Namdeo S, Sinha A K, Singh M N and Awasthi A M 2013 *J. Appl. Phys.* **113** 104101
- [31] Lim Y-F, Chua C S, Lee C J J and Chi D 2014 *Phys. Chem. Chem. Phys.* **16** 25928
- [32] Sivakumar S, van Veggel F C J M and Raudsepp M 2007 *ChemPhysChem* **8** 1677
- [33] Kitahata H, Tadanaga K, Minami T, Fujimura N and Ito T 2000 *J. Sol-Gel Sci. Technol.* **19** 589
- [34] Chen D P, Du Y, Wang X L, Cheng Z X, Dou S X, Lin Z W, Zhu J G and Xu B 2012 *J. Appl. Phys.* **111** 07D913
- [35] Kochur A G, Kozakov A T, Goglev K A and Nikolskii A V 2014 *J. Electron. Spectrosc.* **195** 1
- [36] Zhang R, Chen C, Duan M, Niu L and Jin K 2014 *J. Cryst. Growth.* **390** 56

- [37] Hiramatsu H, Seo W-S and Koumoto K 1998 *Chem. Mater.* **10** 3033
- [38] Han M J, Jiang K, Zhang J Z, Yu W L, Li Y W, Hu Z G and Chu J H 2012 *J. Mater. Chem.* **22** 18463
- [39] Picozzi S, Yamauchi K, Bihlmayer G and Blügel S 2006 *Phys. Rev. B* **74** 094402
- [40] Wang S F, Yang H, Xian T and Liu X Q 2011 *Catalysis Commun.* **12** 625
- [41] Tauc J, Grigorovici R and Vancu A 1966 *Phys. Status Solidi* **15** 627
- [42] Kritayakirana K, Berger P and Jones R V 1969 *Opt. Commun.* **1** 95
- [43] Choi W S, Moon S J, Seo S S A, Lee D, Lee J H, Murugavel P, Noh T W and Lee Y S 2008 *Phys. Rev. B* **78** 054440
- [44] Deng Q L, Zhang J Z, Huang T, Xu L P, Jiang K, Li Y W, Hu Z G and Chu J H 2015 *J. Mater. Chem. C* **3** 8225
- [45] Yao Y B, Liu W C, Mak C L and Wong K H 2011 *AIP Adv.* **1** 032172
- [46] Wu J 2009 *J. Appl. Phys.* **106** 011101
- [47] Dong L and Alpay S P 2012 *J. Electron. Mater.* **41** 3007
- [48] Ryu Y R, Lee T S, Lubguban J A, Corman A B, White H W, Leem J H, Han M S, Park Y S, Youn C J and Kim W J 2006 *Appl. Phys. Lett.* **88** 052103
- [49] Haas C 1962 *Phys. Rev.* **125** 1965
- [50] Park J-S, Jeong J K, Mo Y-G and Kim S 2009 *Appl. Phys. Lett.* **94** 042105
- [51] Manzini S and Modelli A 1989 *J. Appl. Phys.* **65** 2361
- [52] Mamontov Y V and Willander M 1995 *Solid State Electron.* **38** 599
- [53] Altermatt P P, Schenk A and Heiser G 2006 *J. Appl. Phys.* **100** 113714
- [54] Pankove J I and Aigrain P 1962 *Phys. Rev.* **126** 956
- [55] Matsumoto T et al 2013 *Nano Lett.* **13** 4594
- [56] Kobayashi K, Koyama T, Kamo H, Togawa Y, Horibe Y, Cheong S W and Mori S 2012 *Japan. J. Appl. Phys.* **51** 09LE09
- [57] Harunsani M H, Li J, Qin Y B, Tian H T, Li J Q, Yang H X and Walton R I 2015 *Appl. Phys. Lett.* **107** 062905
- [58] Du Y, Wang X L, Chen D P, Dou S X, Cheng Z X, Higgins M, Wallace G and Wang J Y 2011 *Appl. Phys. Lett.* **99** 252107
- [59] Maeda K, Yoshimura T and Fujimura N 2009 *Japan. J. Appl. Phys.* **48** 09KB05
- [60] Scott J F and Dawber M 2000 *Appl. Phys. Lett.* **76** 3801
- [61] Ma Y, Chen X M, Wu Y J and Lin Y Q 2010 *Ceram. Int.* **36** 727